ELSEVIER

Earth and Planetary Science Letters 159 (1998) 35–46

EPSL

# Geodetic measurement of tectonic deformation in the southern Alps and Provence, France, 1947–1994

Gilbert Ferhat [a], Kurt L. Feigl [a,*], Jean-François Ritz [b], Annie Souriau [a]

[a] *UMR 5562, Observatoire Midi-Pyrénées, Centre National de la Recherche Scientifique, 14 Avenue Edouard Belin, 31400 Toulouse, France*

[b] *UMR 5573, Université Montpellier II, Place E. Bataillon, 34095 Montpellier, Cedex 5, France*

Received 28 February 1997; accepted 30 March 1998

**Abstract**

Active deformation at the boundary between the Eurasia and Africa plates varies in style. The belt between the Alpine mountain range and the Mediterranean Sea, for example, differs markedly in its western and eastern parts. In the western part, around southeast France, the mountains are higher, but the seismicity lower, than in the eastern part, around northern Italy and Greece. Yet the inter-plate convergence rate of 6 mm/yr varies by less than 15% between these two areas. To better understand the behaviour of this complex plate boundary, we use geodesy to map the spatial distribution of the deformation. In this paper, we focus on southeast France, a tectonic crossroads between three different domains (Alps, Ligurian Sea, and Massif Central) which exhibits a moderate level of seismicity. Here, the geodetic measurements imply low rates of horizontal deformation. By combining historical triangulation measurements mostly from 1947 to 1983 with Global Positioning System (GPS) surveys in 1993 and 1994, we estimate the rate of angular shear in triangular subnetworks covering the study area. The estimated strain rates in thirteen of nineteen triangles are smaller than their (1 standard deviation) uncertainties of about 0.1 microradian/yr. This value bounds the rate of deformation for a 100-km wide zone in Provence, between Marseilles to the south and the Ventoux massif to the north. The geodetic estimates place an upper bound of 1 to 2 mm/yr on the slip rates of two seismically active structures, the Durance fault and the Nîmes fault, assuming a fault zone ~20 km wide in each case. We also find strain rates as high as $0.20 \pm 0.07$ microradian/yr in three subnetworks near the epicentre of the magnitude 5.3 Haute-Ubaye earthquake in 1959, in a region which includes the higher summits. This may be interpreted either as pure shear with compression oriented NE–SW across this region or right-lateral simple shear along NNW–SSE-trending faults. Given that this earthquake is the only one of its magnitude recorded in the study area during the time interval spanned by the geodetic measurements, we infer that most of the geodetically observed deformation occurs aseismically. On the whole, the geodetic results suggest that the rate of north–south shortening across the 100-km wide study area is not more than 1 or 2 mm/yr, in agreement with kinematic models based on other types of geophysical data. Since this deformation represents only a small part of the convergence rate of 6 mm/yr predicted by the NUVEL-1 model for the entire boundary between the African and Eurasian plates, the remaining deformation must be accommodated elsewhere. This study illustrates how a careful analysis of historical geodetic data can measure the rate of tectonic deformation, even where it is low, and thus meaningfully bound geophysical models. © 1998 Elsevier Science B.V. All rights reserved.

*Keywords:* Alps; neotectonics; deformation; geodesy; Global Positioning System

* Corresponding author. Tel.: +33 (561) 332-940; Fax: +33 (561) 253-205; E-mail: kurt.feigl@cnes.fr

0012-821X/98/$19.00 © 1998 Elsevier Science B.V. All rights reserved.
*PII* S0012-821X(98)00065-X

## 1. Introduction

The theory of global plate tectonics makes two assumptions which are only approximately correct. The first is that the lithosphere behaves as a set of rigid caps (plates) rotating on the surface of a sphere. The second is that their rate of relative rotation is constant on time scales of the order of a million years. Both these approximations break down in plate boundary regions, where episodic earthquakes on faults produce deformation which is neither rigid nor constant in rate. In these regions, the complexity of the faulting, topography, and seismicity suggests that a better mechanical understanding requires observations at length scales shorter than the characteristic size of a continent and at time scales shorter than the recurrence interval for large earthquakes. This poses the problem of how the crustal deformation is distributed in time and space. Precise geodetic measurements can help improve our understanding of the shortcomings of these approximations mapping the rate of deformation on the continents.

In approaching this problem, we note a serious trade-off between spatial and temporal resolution. We choose to favour the former at the expense of the latter in this paper. Increasing spatial resolution requires a geodetic network with closely spaced stations. To save time and expense, we choose to remeasure an existing triangulation network by GPS rather than install a new set of points and wait for them to move. These two choices lead to a map of deformation at the spatial scale of several tens of kilometres and a temporal scale of four decades. Our approach contrasts markedly with a network of continuously recording GPS receivers, which samples the deformation field, much more coarsely in space (several hundred kilometres between stations) but much more frequently (position estimates once per day). As a consequence, however, our approach inherits two (minor) drawbacks from the triangulation surveys. The existing networks are regional, not global, because triangulation requires visibility along the line of sight between stations, thereby degrading precision over long distances. Furthermore, triangulation measurements are not as precise as GPS, primarily because of optical refraction in the lowermost atmosphere. The major advantage, of course, is that our approach can estimate the rate of deformation without waiting any longer. In this paper, we use the fine-scale approach, favouring spatial resolution, to focus on a small, but active, part of a complex plate boundary.

In the western Mediterranean, Africa and Eurasia are colliding with a convergence rate of $6.2 \pm 0.5$ mm/yr in the direction N17°W $\pm$ 9°, assuming two rigid plates and constant velocity over the last three million years [1,2]. A relative lack of seismicity, combined with space geodetic measurements, suggest that northern Europe is currently deforming quite slowly [3,4]. The central and eastern parts of the Mediterranean region, however, exhibit higher rates of deformation, in the presence of sustained seismicity, particularly in Greece [5–7], Turkey [8], and Italy [9]. The western part of the Mediterranean coast of Europe, on the other hand, appears to be less active. Here, the most pertinent geodetic observation involves the Satellite Laser Ranging station at Grasse (near Nice) in southeast France (Figs. 1 and 2). Its velocity is $3 \pm 2$ mm/yr of southward displacement with respect to northern Europe [4] (Fig. 3). In the northern Alps, geodetic data have been interpreted in terms of some 4 mm/yr of horizontal shortening in the Jura range [10,11] and 3–5 mm/yr of shortening between the Belledonne range and the subalpine chains [12]. Such displacement rates, when distributed over small geodetic networks, imply strain rates in excess of $2 \times 10^{-7}$/yr. These rates are startling because they are as high as those observed around the active trace of the San Andreas fault system in California [13].

In this paper, we map crustal deformation in southeast France during this century. The study area lies at the crossroads between three different tectonic domains: (1) the high, active Alpine mountain range; (2) the relatively undeformable Massif Central; and (3) the relatively malleable offshore oceanic basin of the Ligurian Sea (Fig. 1). In the study area, the level of seismic activity is moderate (Fig. 2). The largest known and most recent earthquake is the Lambesc event of 1909 with intensity IX (on the MSK scale [14]), attributed to the Trévaresse thrust fault [15,16]. Several large (intensity VIII–IX) earthquakes also occurred near Vésubie, north of Nice, in 1564, 1618, and 1644 [16]. The largest earthquakes recorded instrumentally are the 1959 magnitude 5.3 Haute-Ubaye event and the 1963 magnitude

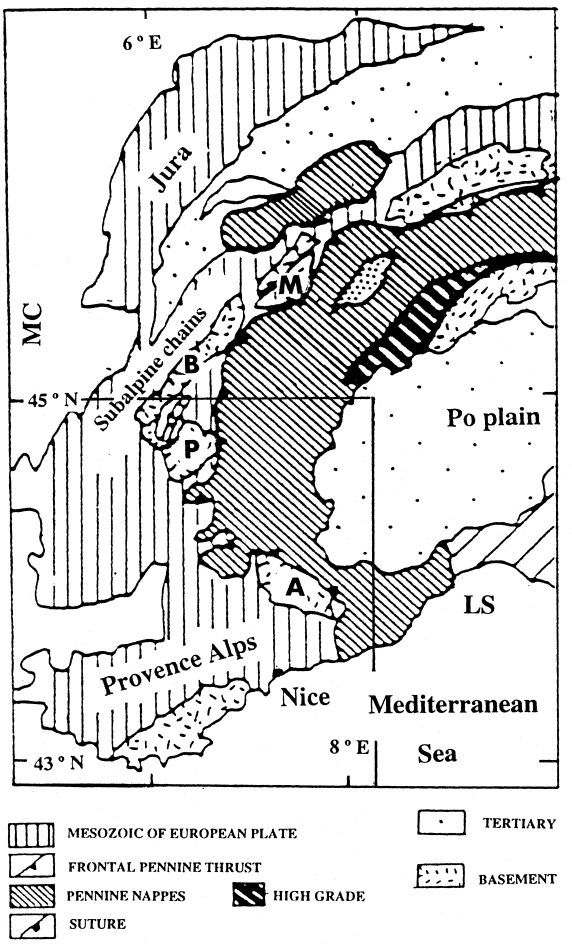


Fig. 1. Tectonic setting: $P$ = Pelvoux; $A$ = Argentera; $M$ = Mont Blanc; $B$ = Belledonne; $MC$ = Massif Central; $LS$ = Ligurian Sea. Study area outlined by small rectangle. Figure redrawn from Ref. [45].

5.6 event in the Ligurian Sea [16,17]. The geodetic network spans the Provence domain (Fig. 3), which is characterized by strike-slip faults striking NE–SW (Durance, Nîmes, and Cévennes) and thrusts trending E–W (Ventoux, Lure, Lubéron, Trévaresse, and Costes). In the northeastern part of the study area, the Embrunais–Ubaye region includes folds and faults striking NNW–SSE (Durance–Serenne–Roburent). The eastern edge of the study area includes the outer folded parts of the Digne and Castellane *nappes*. Field observations and palaeostress determinations from fault slip data analysis suggest that the tectonic regime in the study area is characterized by north–south compression [18–20]. In this paper, we examine the historical geodetic data set, the longest available instrumental geophysical time series, to measure the rate of tectonic deformation.

The objectives of this study are four in number. First, to validate a geodetic technique for measuring low rates of crustal deformation from a heterogeneous triangulation survey from the late 1940s. Second, to estimate the fraction of the inter-plate convergence accommodated in our study area. Third, to estimate the amount of deformation accommodated in the absence of earthquakes. Fourth, to test the kinematic consequences on short time scales of geophysical models intended to explain long-term tectonic deformation in the area.

## 2. Data selection

We analyze two types of geodetic data at 17 geodetic sites measured at least twice by triangulation or GPS (Table 1). The early surveys are first- and second-order triangulation observations performed by the French national survey agency, *Institut Géographique National* (IGN), primarily during campaigns in 1947–1952 and 1981–1983 with a few measurements between 1887 and 1931. The early first-order campaigns before 1947 used azimuth circles and reduced the eccentric observations to the primary monument. Consequently, the standard deviation of a direction measurement is 1.3–2.0 s of arc. The later first- and second-order campaigns used modern theodolites permitting an uncertainty of 0.7–1.0 s of arc or about 3.0–4.8 microradians (μrad). Further details on the historical data are described elsewhere [21,22].

The GPS data come from two separate observation campaigns in 1993 and 1994, both tied to the International Terrestrial Reference Frame site at Grasse (Fig. 3). The first involves 8-h observation sessions in September 1993, during the first occupation of a network called *Alpes93* with ∼50 km spacing between stations designed to capture tectonic deformation [23]. The second campaign surveyed the new French national geodetic network, called *Réseau de Base Français* (RBF94) and installed by IGN in 1994 [24]. We analyze the GPS data from the *Alpes93* and RBF94 campaigns as well as five permanent stations

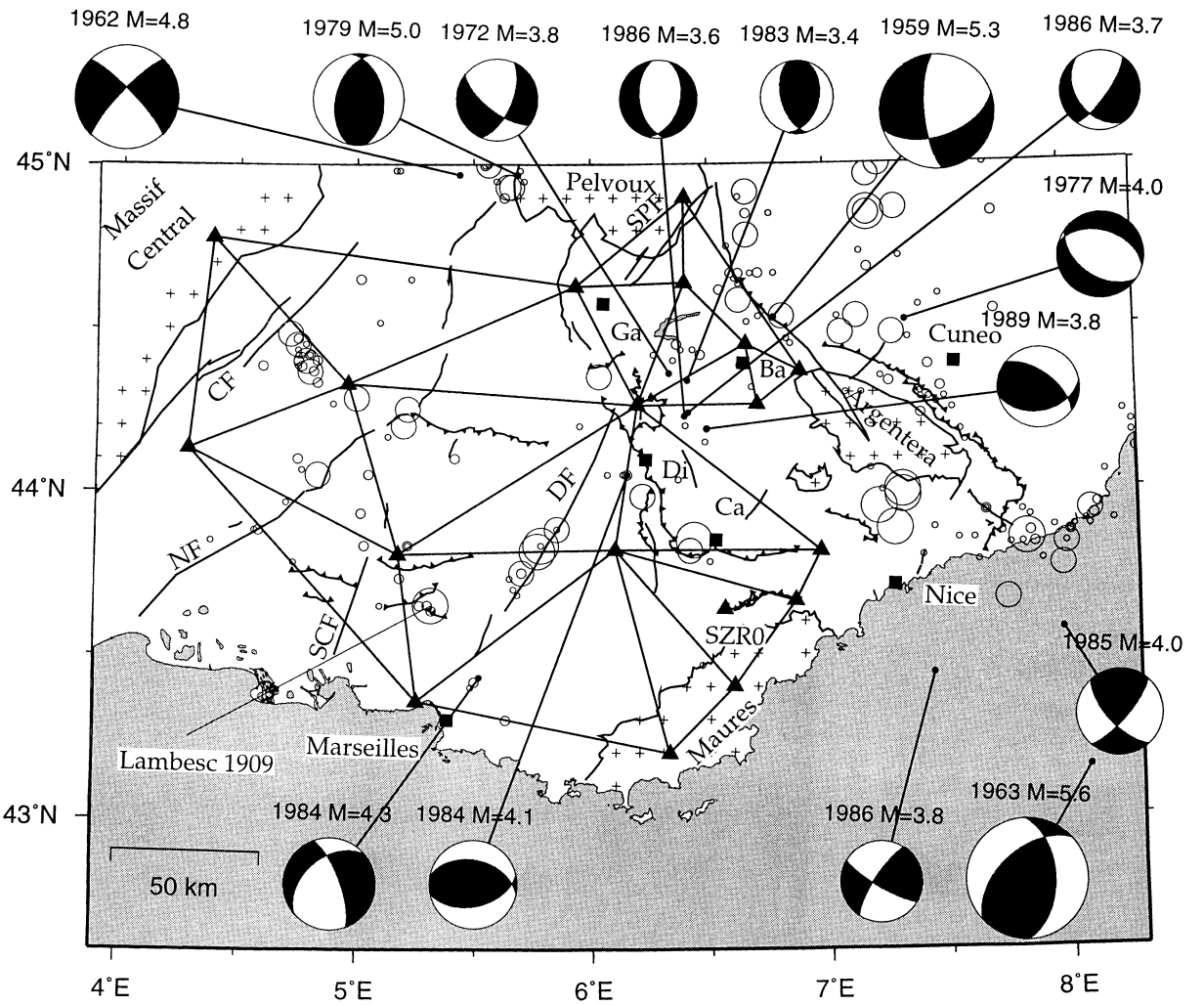


Fig. 2. Seismicity superimposed on the geodetic network. Circles denote events between 1000 and 1994 with MSK intensity ranging from V to IX [36]. Focal mechanisms, showing the lower hemisphere, and labelled with approximate local (body-wave) magnitude (>3.5) and span 1959 through 1986 [36,44]. *SCF* = Salon–Cavaillon fault; *Ba* = Barcelonnette. Other abbreviations as in Fig. 3.

in Europe (Madrid, Spain; Matera, Italy; Graz, Austria; Wettzell, Germany; and Hersmonceux, England) in the International GPS Service (IGS) network.

We analyze the data using the GAMIT software [25] with standard procedures [13]. For each signal, the linear combination (LC) that removes first-order ionospheric phase delays is formed from the two GPS frequencies [26]. Double difference LC phase residuals are inspected manually for cycle slips in the phase data, although virtually all cycle slips can be detected and corrected by automatic algorithms. The GPS data are grouped as daily network solutions, with about thirteen stations in each solution, holding fixed the coordinates of the IGS stations and the satellite ephemerides calculated at the Center for Orbit Determination in Europe [27]. Root mean square scatter (or 'RMS repeatabilities') for stations with multiple occupations are 5.4 mm, 7.1 mm, and 13.9 mm, respectively, in the north, east, and vertical components of the *Alpes93* vectors and are less than 5.7 mm, 6.0 mm, and 30 mm in the north, east and vertical components of the RBF94 vectors [22].

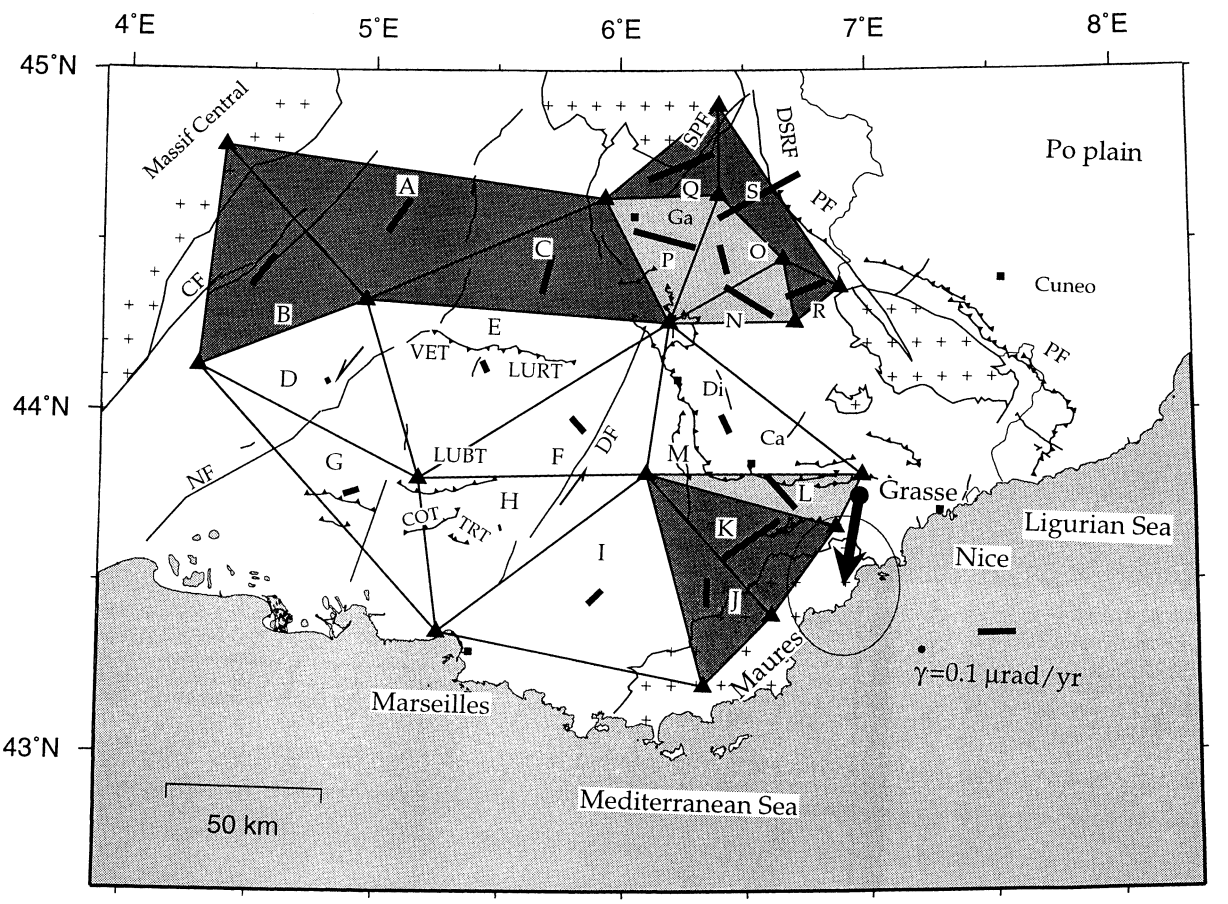


Fig. 3. Map showing geodetic network stations measured on at least two different dates for which we can estimate a velocity (solid triangles). The mesh is a Delaunay triangulation connecting these points. Within each such subnetwork, the bar indicates the azimuth $\theta$ of the maximum compressive strain. The length of the bar is proportional to the ('total') shear strain rate $\dot{\gamma}$. These two parameters classify the subnetworks into three categories, distinguished by their shading: white = negligible deformation $\dot{\gamma} \leq 0.05$ μrad/yr; dark grey = NE–SW compression with $\dot{\gamma} > 0.08$ μrad/yr and $\theta$ between N0° and N75°E; light grey = NW–SE compression with $\dot{\gamma} > 0.08$ μrad/yr and $\theta$ between N10°W and N75°W. The Penninic front is abbreviated *PF*. Faults are shown as heavy lines with triangular teeth on the underthrust side, including: *CF* = Cévennes fault; *NF* = Nîmes fault; *DF* = Durance fault; *COT* = Costes thrust; *LURT* = Lure thrust; *TRT* = Trevaresse thrust; *LUBT* = Lubéron thrust; *SPF* = NE–SW-trending faults south of the Pelvoux massif; *VET* = Ventoux thrust; *DSRF* = Durance–Serenne–Roburent fault. Relatively rigid blocks are shown with crosses. Squares denote cities: *Di* = Digne; *Ca* = Castellane; *Ga* = Gap. Arrow shows the velocity ($3.3 \pm 2.5$ mm/yr at N169.4°W ± 35.5°) of the Grasse site relative to northern European sites from space geodetic measurements between 1983 and 1992 [4].

## 3. Estimation procedure

To estimate the strain rates, we use the forward modelling network deformation analysis software package to adjust the network [28,29]. For each station, we can estimate as many as four parameters: the two horizontal components of both the position and velocity vectors in a so-called 'free network' solution. The velocity does not vary with time.

We pay particular attention to the occupation history of each benchmark. For example, we do not estimate a velocity for a station with only a single occupation. We avoid 'tie' measurements by ensuring that the GPS benchmark coincides with the triangulation benchmark. Furthermore, multiple GPS occupations of a given benchmark are never separated by more than a few days in our solution.

Table 1
Station names, coordinates, number of directions and year of observation

| Station | Long. (°E) | Lat. (°N) | *N* | 1st obs. | 2nd obs. |
|---|---|---|---|---|---|
| CBR9 | 4.3 | 44.1 | 27 | 1903, 1924 | 1993 |
| RPA9 | 4.4 | 44.8 | 6 | 1947 | 1993 |
| SUN4 | 5.0 | 44.3 | 15 | 1947 | 1994 |
| LUBA | 5.2 | 43.8 | 26 | 1901, 1930, 1947 | 1993 |
| RVE9 | 5.3 | 43.4 | 5 | 1887, 1930 | 1994 |
| SXL4 | 5.9 | 44.6 | 6 | 1905, 1927, 1949 | 1983, 1994 |
| SXQ5 | 6.1 | 43.8 | 7 | 1952 | 1994 |
| SYOS | 6.2 | 44.3 | 17 | 1903, 1930, 1949 | 1981, 1994 |
| SYU5 | 6.3 | 43.2 | 4 | 1952 | 1994 |
| 11414 | 6.4 | 44.6 | 21 | 1949 | 1983 |
| 11409 | 6.4 | 44.9 | 28 | 1949 | 1983 |
| SZS4 | 6.6 | 43.4 | 17 | 1952 | 1994 |
| 11417 | 6.7 | 44.4 | 22 | 1949 | 1981 |
| 11418 | 6.7 | 44.3 | 38 | 1949 | 1981 |
| CABR | 6.9 | 43.7 | 7 | 1952 | 1993 |
| 11419 | 6.9 | 43.4 | 17 | 1949 | 1981 |
| CHEO | 7.0 | 43.8 | 40 | 1948, 1952 | 1993 |

First observations are always horizontal angles. Second observations are also horizontal angles in 1981 or 1983, but GPS measurements in 1993 or 1994.

The vertical component of the position coordinate (ellipsoidal elevation) for each station remains fixed to its GPS-derived value. For stations never occupied by GPS, we retain the relative height differences estimated by IGN from spirit and/or trigonometric levelling, correcting for geoid undulations using values interpolated from a model [30]. We do not correct the triangulation observations for deflection of the vertical, an approximation which is unlikely to cause significant errors in the estimates of strain rate.

From the resulting velocity estimates, which are undetermined in scale and orientation, we calculate the angular shear strain rates over triangular subnetworks (Fig. 3). This technique has also been applied to a similar data set involving historical triangulation and modern GPS observations [31].

The angular shear rates are defined by convention [32]:

$$\dot{\gamma}_1 = \dot{\mathbf{E}}_{ee} - \dot{\mathbf{E}}_{nn} \tag{1}$$

$$\dot{\gamma}_2 = 2\dot{\mathbf{E}}_{en} \tag{2}$$

where $\dot{\mathbf{E}}$ is the conventional strain rate tensor, that is the symmetric part of the gradient of the velocity field, and the subscripts 'e' and 'n' denote eastward and northward components, respectively. The shear rate parameter $\dot{\gamma}_2$ measures the decrease in the right angle between a ray pointed north and one pointed east, as sketched previously [33]. This decrease can be attributed to either right-lateral shear across a vertical fault striking east or to left-lateral shear across a fault striking north. Similarly, $\dot{\gamma}_1$ measures the decrease in the right angle between rays pointing northwest and northeast, due to right-lateral shear on a fault striking N45°W or left-lateral shear on a fault striking N45°E. These parameters can also be estimated directly from angle changes between repeated measurements of direction [32,34], but such an approach does not suit the extremely heterogeneous nature of the Alpine geodetic data set.

As an alternative representation, we also calculate the maximum ('total') shear strain rate $\dot{\gamma}$ and the azimuth $\psi$ of the vertical plane on which it occurs using the expressions:

$$\dot{\gamma} = \sqrt{\dot{\gamma}_1^2 + \dot{\gamma}_2^2} \tag{3}$$

$$\tan 2\psi = \frac{\dot{\gamma}_1}{\dot{\gamma}_2} \tag{4}$$

In Fig. 3, we show the azimuth $\theta = \psi - 45°$ to provide the orientation of the axis of the most compressive principal strain rate, called the 'P-axis' by seismologists.

$$\theta = \tfrac{1}{2}\,\mathrm{atan}\,(-\dot{\gamma}_2/\dot{\gamma}_1) \quad \text{if } \dot{\gamma}_1 > 0 \tag{5a}$$

$$\theta = \tfrac{1}{2}\,\mathrm{atan}\,(-\dot{\gamma}_2/\dot{\gamma}_1) - \pi/2 \quad \text{if } \dot{\gamma}_1 < 0 \text{ and } \dot{\gamma}_2 > 0 \tag{5b}$$

$$\theta = \tfrac{1}{2}\,\mathrm{atan}\,(-\dot{\gamma}_2/\dot{\gamma}_1) + \pi/2 \quad \text{if } \dot{\gamma}_1 < 0 \text{ and } \dot{\gamma}_2 < 0 \tag{5c}$$

Both $\psi$ and $\theta$ are azimuths measured in degrees clockwise from north. The numerical values of all four parameters and their $1\sigma$ uncertainties appear in Table 2.

The advantage of parameterizing the gradient of the velocity field in terms of two angular shear strain rates is that we can separate them from the rates of dilatation and rotation. We cannot resolve dilatation and rotation because we lack geodetic control on the scale and orientation of the network. This is because

Table 2
Components of angular shear rates $\dot{\gamma}_1$ and $\dot{\gamma}_2$, total shear rate $\dot{\gamma}$ and azimuth $\theta$ of the P-axis in degrees clockwise from north

| Subnetwork | $\dot{\gamma}_1$ (μrad/yr) | $\dot{\gamma}_2$ (μrad/yr) | $\dot{\gamma}$ (μrad/yr) | $\theta$ (°) |
|---|---|---|---|---|
| A | $0.04 \pm 0.12$ | $-0.10 \pm 0.14$ | $0.11 \pm 0.14$ | $35.1 \pm 31.5$ |
| B | $0.03 \pm 0.10$ | $-0.10 \pm 0.12$ | $0.10 \pm 0.12$ | $37.7 \pm 28.4$ |
| C | $0.09 \pm 0.11$ | $-0.05 \pm 0.10$ | $0.11 \pm 0.11$ | $15.2 \pm 27.9$ |
| D | $-0.007 \pm 0.061$ | $-0.01 \pm 0.06$ | $0.01 \pm 0.06$ | $62.3 \pm 141$ |
| E | $0.02 \pm 0.05$ | $0.02 \pm 0.05$ | $0.03 \pm 0.05$ | $-24.6 \pm 45.1$ |
| F | $0.006 \pm 0.063$ | $0.05 \pm 0.10$ | $0.05 \pm 0.10$ | $-41.8 \pm 34.1$ |
| G | $-0.04 \pm 0.09$ | $-0.03 \pm 0.10$ | $0.04 \pm 0.09$ | $72.2 \pm 61.7$ |
| H | $-0.006 \pm 0.081$ | $0.005 \pm 0.058$ | $0.008 \pm 0.074$ | $72.5 \pm 236$ |
| I | $-0.001 \pm 0.05$ | $-0.05 \pm 0.07$ | $0.05 \pm 0.07$ | $45.4 \pm 24.2$ |
| J | $0.08 \pm 0.07$ | $-0.01 \pm 0.07$ | $0.08 \pm 0.07$ | $2.32 \pm 27.3$ |
| K | $-0.07 \pm 0.07$ | $-0.16 \pm 0.08$ | $0.18 \pm 0.08$ | $56.7 \pm 11.2$ |
| L | $0.02 \pm 0.13$ | $0.12 \pm 0.12$ | $0.12 \pm 0.12$ | $-40.5 \pm 31.2$ |
| M | $0.03 \pm 0.07$ | $0.04 \pm 0.07$ | $0.05 \pm 0.07$ | $-25.0 \pm 40.9$ |
| N | $-0.06 \pm 0.07$ | $0.14 \pm 0.09$ | $0.15 \pm 0.09$ | $-57.4 \pm 13.6$ |
| O | $0.07 \pm 0.08$ | $0.04 \pm 0.05$ | $0.08 \pm 0.08$ | $-13.8 \pm 21.0$ |
| P | $-0.14 \pm 0.09$ | $0.09 \pm 0.07$ | $0.17 \pm 0.09$ | $-74.3 \pm 13.0$ |
| Q | $-0.14 \pm 0.09$ | $-0.13 \pm 0.09$ | $0.19 \pm 0.09$ | $68.5 \pm 13.6$ |
| R | $-0.09 \pm 0.12$ | $-0.08 \pm 0.12$ | $0.11 \pm 0.12$ | $69.2 \pm 30.1$ |
| S | $-0.14 \pm 0.10$ | $-0.17 \pm 0.07$ | $0.20 \pm 0.07$ | $60.1 \pm 12.0$ |

Subnetworks A to S are shown in Fig. 3.

the triangulation surveys do not include precise observations of distance or azimuth. As a consequence, we can resolve only angular changes measured by the parameters $\dot{\gamma}_1$ and $\dot{\gamma}_2$. The disadvantage of this parameterization is that it is difficult to interpret unambiguously. In particular, it cannot distinguish pure shear from simple shear without additional information.

## 4. Geodetic estimates of strain rate

To evaluate the robustness of our solutions to the estimation strategy, we have performed a suite of sensitivity tests on the following issues: (1) a priori values of the vertical component of station position; (2) correcting for the deflection of the vertical where possible; and (3) choice of fixed stations or a 'free network' adjustment. None of these perturbations alters the estimated values of $\dot{\gamma}_1$ and $\dot{\gamma}_2$ by more than about a third of their stated uncertainty [22].

We have rejected one estimate of shear strain rate higher than 0.3 μrad/yr, half the typical value for rapid shear across the San Andreas fault in California [35]. Such a high rate does not seem reasonable in the Alps, where the relative speed between the bounding plates is roughly eight times slower than in California. It occurred in the solution for the 1952 and 1993–1994 surveys, where we found unreasonably high values in all the triangles involving station SZR0 (Fig. 2). Either the benchmark is unstable or the tie vector between the survey flag and the benchmark is incorrect. To avoid confusion, we have omitted this station from the solution shown here.

## 5. Interpretation

The maximum shear strain rate $\dot{\gamma}$ is significantly different from zero (with 68% confidence) in only six of nineteen subnetworks (Table 2). The uncertainty is typically about 0.1 μrad/yr, which corresponds to 1 mm/yr of shearing motion across a zone 10 km wide.

To visualize the shear strain rates, we plot them on a map in Fig. 3. We group the subnetworks into three categories according to the values of the maximum shear strain rate $\dot{\gamma}$ and the azimuth $\theta$ of the compressive principal axis of the strain rate tensor.

### 5.1. Negligible deformation (white areas in Fig. 3)

In subnetworks D–I, and M, the value of the maximum shear strain rate $\dot{\gamma}$ is 0.05 μrad/yr and smaller than its uncertainty. This area includes the Ventoux massif, the Lubéron region, and the Castellane *nappe*. Here, the rate of deformation is too small to detect with our geodetic data set. In other words, the uncertainty of 0.03 μrad/yr for $\dot{\gamma}$ averaged over a polygon including the seven triangles provides an upper bound on the deformation rate in this region. This upper bound applies to the Nîmes and Durance strike-slip faults as well as the Ventoux–Lure and Lubéron–Costes–Trévaresse thrust faults, all of which are supposed to be active.

The Durance fault, the inferred site of several historical earthquakes with MSK intensity greater than VII [16,36], passes through triangles F and H for which the estimated shear strain rates do not exceed $0.1 \pm 0.1$ μrad/yr. If this left-lateral strike-slip fault had a high slip rate, we would expect to see simple shear as positive values of $\dot{\gamma}_1$ rather than the insignificant values of $0.006 \pm 0.06$ μrad/yr and $-0.007 \pm 0.08$ μrad/yr we estimate in triangles F and H, respectively. Our geodetic results confirm those of a previous study which did not detect significant motion in a separate, small-aperture geodetic network spanning the fault surveyed by triangulation and trilateration in 1986, 1987, 1988, and 1989, and by GPS in 1990 [37]. These estimates imply that the long-term slip rate on the Durance fault is unlikely to exceed 2 mm/yr, assuming a fault zone 20 km wide.

Similarly, the Nîmes fault cuts across triangles D and G. The estimated maximum shear strain rate does not exceed 0.04 μrad/yr in either of these triangles. Left-lateral simple shear on this NE–SW-trending strike-slip fault [38] would produce positive values of $\dot{\gamma}_1$. This result implies that there is no significant aseismic slip occurring on the fault or interseismic strain accumulating across it. The uncertainty of the geodetic estimate places an upper bound of about 2 mm/yr on the present-day slip rate for this fault, again assuming a fault zone 20 km wide. This result is also consistent with the low level of present-day activity and the long earthquake recurrence interval inferred from palaeoseismological studies [39,40]. At its northern end, the left-lateral Nîmes fault meets a N–S-trending fault zone in the folded and thrust Ventoux massif (triangle E). Here, our geodetic estimates of shear rate are not significantly different from zero, although the negative value of $\dot{\gamma}_2$ in triangle E is compatible with either right-lateral simple shear on a north-striking fault or left-lateral simple shear on an east-striking fault. Taking into account the relationships between the various faults and thrusts in this area, we infer long repeat intervals for large earthquakes on E–W-trending structures such as the Lubéron, Costes, and Trévaresse thrusts (Fig. 2).

### 5.2. NE–SW compression (dark grey areas in Fig. 3)

Seven of the nineteen subnetworks have a compressional axis with azimuth $\theta$ between N15ºE and N75ºE and a maximum strain rate $\dot{\gamma}$ larger than 0.08 μrad/yr, but not necessarily larger than its uncertainty. These subnetworks appear to be undergoing compression along an axis oriented roughly NE–SW, as we will discuss in three distinct areas.

Subnetworks Q–R show maximum shear strain rates between 0.10 and 0.20 μrad/yr, the fastest we observe in our study area, with a compressive axis oriented consistently between N60ºE and N70ºE. Before interpreting these relatively rapid rates, we consider two geodetic caveats. First, these subnetworks involve only two triangulation surveys in 1949 and again in 1981–1983. We have no GPS measurements at these sites (Table 1). Second, the earlier survey uses eccentric reductions to correct the direction lists, while the second survey considers the theodolite at the standpoint and the target flag at the forepoint as separate geodetic points, each with their own coordinates. This difference in observing protocol means that the estimated values of the shear rates depend heavily on the measurements between standpoint and forepoint used in the eccentric reduction. Having no other information, we assume these measurements to have zero uncertainty.

To interpret these rapid rates near the Penninic front, between the Pelvoux and Argentera massifs, we note that the magnitude 5.3 Haute-Ubaye earthquake occurred in 1959, within the geodetic observation interval [17]. Could the signal be coseismic? To produce the observed shear strain rates would require some 6 cm of displacement within the geodetic

subnetwork in the 33 years between surveys, assuming right-lateral strike-slip on a fault striking N10ºW, as indicated by the focal mechanism [17]. Yet the epicentre has been located over 10 km from the nearest geodetic benchmark (site 11,417). Moreover, the fault most likely responsible for the earthquake, the Durance–Serenne–Roburent fault, according to the structural map [41], is even farther from subnetworks Q–S. At these large distances, the coseismic displacement is of the order of 1 mm, not large enough to explain the observed geodetic signal. We conclude, therefore, that the 1959 earthquake alone did not produce the deformation recorded by the geodetic network.

The strain rates in subnetworks Q–S are consistent with interseismic strain which can be interpreted in two different ways. The first possibility involves right-lateral simple shear along NNW–SSE-trending faults, as mapped in the field [42,43]. The second possibility involves compressive pure shear strain oriented roughly NE–SW, perpendicular to the Penninic front. Although we cannot easily distinguish between these two possibilities, we prefer the latter, because the rapid strain rates throughout the Penninic front coincide with higher seismicity than elsewhere in our study area (Fig. 2).

In the northwest part of the network, we also find compressive axes oriented NE–SW in triangles A–C. Although the value of $\dot{\gamma}$ is smaller than its uncertainty in each individual triangle, the similarity of the strain rates in three neighbouring triangles increases our confidence in the geodetic estimates. Here the compressive axis is slightly more northerly ($\theta$ between N15ºE and N38ºE) and the shear strain rate slightly slower ($\dot{\gamma}$ of 0.10–0.11 μrad/yr) than in subnetworks Q–S. Although these observations are compatible with N–S shortening squeezing soft material between the hard crystalline rocks in the external Alps and those in the Massif Central, they are difficult to reconcile with activity on NE–SW-trending strike-slip faults such as the Cévennes fault or the N–S-trending fault between Ventoux and Pelvoux.

Further south, we also find NE–SW-directed compression in triangle K, covering part of the Maures massif and the Valensole plateau. Here, the estimated rates of angular shear are $\dot{\gamma}_1 = -0.071 \pm 0.069$ μrad/yr and $\dot{\gamma}_2 = -0.16 \pm 0.08$ μrad/yr. The former is marginally significant; the latter is significantly different from zero with 97% confidence. The principal compressive axis is oriented $\theta$ = N57ºE ± 11º. Such movement suggests that the Castellane *nappe* drives southwest into the rigid Maures massif. To the west, in subnetwork J, the principal compressive axis is more northerly, with $\theta$ = N2ºE ± 27º, but the shear strain rate is only marginally significant, $\dot{\gamma} = 0.08 \pm 0.07$ μrad/yr.

### 5.3. NW–SE compression (light grey areas in Fig. 3)

In the Embrunais–Ubaye region between Gap and Barcelonnette, a group of three triangles, P, O, and N, show shear strain rates in excess of 0.08 μrad/yr with the compressive axis in the northwest quadrant. This orientation contrasts sharply with that observed in the neighbouring groups of subnetworks (A + B + C) and (Q + R + S). This significant change in the deformation field over a distance of less than 50 km is difficult to explain. It is reminiscent of, but not compatible with, a sharp change in the orientation of P-axes observed in the focal mechanisms of small earthquakes near this area [44] (their zone 'SE'). A speculative explanation would involve some extensional motion on N–S-trending faults in this area.

The triangular subnetwork L also shows compression oriented roughly northwest ($\theta$ = N41ºW ± 31º) and an intermediate shear strain rate ($\dot{\gamma} = 0.12 \pm 0.12$ μrad/yr). Yet unlike the other subnetworks, triangle L sits in isolation with a P-axis oriented quite differently from its neighbours'. Such an orientation is difficult to reconcile with N–S compression in the Castellane *nappe*, as expected from the E–W trend of thrust fault mapped in this area [19]. It is also difficult to reconcile with the deformation observed in subnetwork K, just to the south. Nor can we reconcile the deformation observed in subnetwork L with the movement of the continuously recording GPS station at Grasse toward the west at some 2 mm/yr with respect to a reference frame fixed on stable Eurasia (E. Calais, written commun., 1997). Perhaps the most prudent interpretation is to discount the statistical significance of the geodetic estimate of strain rate in triangle L by noting that the uncertainty is as large as the value.

## 6. Conclusions

We have shown that a rigorous analysis of historical data in a tightly spaced geodetic network can provide useful geophysical information, even in areas of relatively low rates of deformation. Although most of the geodetic triangles yield strain rate estimates which are not significantly different from zero, they tend to support the kinematic model proposed previously on the basis of other geological and geophysical observations [18,19]. Eight of nineteen geodetic subnetworks indicate compression oriented roughly NE–SW. The region between the Pelvoux and Argentera massifs appears to be deforming more rapidly than elsewhere in the study area. Here, the axis of maximum compression is oriented northeast, roughly perpendicular to the Penninic front. Further south, the Maures massif behaves as a rigid block, moving northeastward relative to the Alpine arc. Still, four other subnetworks do not fit this pattern. Elsewhere in the Provence region, the estimated strain rates and their uncertainties are low, both less than 0.1 μrad/yr. Interpreted as interseismic deformation accumulating on locked faults between large earthquakes, these values imply long-term fault slip rates slower than 1–2 mm/yr. Taken as a whole, our geodetic solution suggests that the rate of north–south shortening across the study area is not more than 1 or 2 mm/yr. Most of this deformation appears to occur aseismically within the time interval spanned by the measurements. It contributes to the convergence rate of 6 mm/yr predicted by the NUVEL-1 model for the entire boundary between the African and Eurasian plates. Furthermore, the geodetic estimates suggest spatial variations in the crustal deformation field over distances as short as 50 km, a possibility which reflects the intricate structural geometry at this plate boundary. For this reason, wide-aperture geodetic networks may spatially undersample the contemporary deformation field.

## Acknowledgements

We wish to thank Danan Dong for generously sharing and supporting his Forward Modelling Network Deformation Analysis software. Georges Ferhat and Vincent Deschaux tirelessly carried batteries to mountain tops. In addition, we thank all the members of the 'GPS-Alpes' working group [23] for collecting the 1993 GPS data under difficult conditions as well as the surveyors of the Institut Géographique National (IGN). We appreciate the conscientious efforts of IGN in recovering the historical data. The *Programme National en Risques Naturels de l'INSU* provided funding. ***[FA]***

## References

[1] C. DeMets, R.G. Gordon, D.F. Argus, S. Stein, Current plate motions , Geophys. J. Int. 101 (1990) 425–478.
[2] C. DeMets, R.G. Gordon, D.F. Argus, S. Stein, Effect of the recent revisions to the geomagnetic reversal time scale on estimates of current plate motions, Geophys. Res. Lett. 21 (1994) 2191–2194.
[3] D.E. Smith, R. Kolenkewicz, J.W. Robbins, P.J. Dunn, M.H. Torrence, Horizontal crustal motion in the central and eastern Mediterranean inferred from satellite laser ranging measurements, Geophys. Res. Lett. 21 (1994) 1979–1982.
[4] R. Noomen, T.A. Springer, B.A.C. Ambrosius, K. Herzerberger, D.C. Kuijper, G.-J. Mets, B. Overgaauw, K.F. Wakker, Crustal deformations in the Mediterranean area computed from SLR and GPS observations, J. Geodyn. 21 (1996) 73–96.
[5] H. Billiris, D. Paradissis, G. Veis, P. England, W. Featherstone, B. Parsons, P. Cross, P. Rands, M. Rayson, P. Sellers, V. Ashkenazi, M. Davison, J. Jackson, N. Ambraseys, Geodetic determination of tectonic deformation in central Greece from 1900 to 1988, Nature 350 (1991) 124–129.
[6] A. Rigo, W.G. Corinthe, Active normal faults in the Gulf of Corinth (Greece): microseismic and geodetic observations, Ann. Geophys. 12 (Suppl. I) (1994) C70.
[7] A. Rigo, Étude sismotectonique et géodésique du Golfe de Corinthe (Grèce), France, Thèse de Doctorat de 3ème cycle, Univ. Paris VII, 1994, 281 pp.
[8] M.B. Oral, R.E. Reilinger, M.N. Toksöz, R.W. King, A.A. Barka, I. Kinik, O. Lenk, Global Positioning System offers evidence of plate motions in Eastern Mediterranean, Eos 76 (1995) 9–11.
[9] E. Mantovani, D. Albarello, C. Tamburelli, M. Viti, Tectonic interpretation of large scale geodetic measurements (VLBI, SLR) in the Central Mediterranean region: constraints and uncertainties, Ann. Geofis. 38 (1995) 67–84.
[10] F. Jouanne, G. Ménard, D. Joualt, Present-day deformation of the French northwestern Alps/southern Jura mountains: comparison between historical triangulations, Geophys. J. Int. 119 (1994) 151–165.
[11] F. Jouanne, G. Ménard, X. Darmendrail, Present-day vertical displacements in the north-western Alps and southern Jura mountains: Data from leveling comparisons, Tectonics 14 (1995) 606–616.
[12] J. Martinod, F. Jouanne, J. Taverna, G. Ménard, J.F. Ga-

mond, X. Darmendrail, J.C. Notter, C. Basile, Present-day deformation of the Dauphiné Alpine and Subalpine massifs (SE France), Geophys. J. Int. 127 (1996) 189–200.
[13] K.L. Feigl, D.C. Agnew, Y. Bock, D. Dong, A. Donnellan, R.W. King, B.H. Hager, T.A. Herring, D.D. Jackson, T.H. Jordan, S. Larsen, K.M. Larson, M.H. Murray, Z. Shen, F.H. Webb, Space geodetic measurement of crustal deformation in central and southern California, 1984–1992, J. Geophys. Res. 98 (1993) 21677–21712.
[14] S. Medvedev, W. Sponheuer, W. Karnik, Seismic intensity scale version 1964, Iena, 1964, 48 pp.
[15] J. Vogt, B. Cadiot, J. Delaunay, G. Faury, J. Goguel, B. Massinon, D. Mayer-Rosa, C. Weber, Les Tremblements de Terre en France, B.R.G.M., Orléans, 1979, 220 pp.
[16] J. Lambert, Q. Levret-Albaret, Mille ans de séismes en France: catalogue d'épicentres, paramètres et références, Presses Académiques, 1996, 75 pp.
[17] G. Ménard, Structure et cinématique d'une chaîne de collision — les Alpes occidentales et centrales, Thèse d'Etat, Univ. J. Fourier, Grenoble, 1988, 268 pp.
[18] P. Combes, La tectonique récente de la Provence occidentale: microtectonique, caractéristiques dynamiques et cinématiques. Méthodologie de zonation tectonique et relation avec la sismicité, Ph.D. thesis, Univ. Louis Pasteur, Strasbourg, 1984, 182 pp.
[19] J.F. Ritz, Evolution du champ de contrainte dans les Alpes du Sud depuis la fin de l'Oligocène, implications sismotectoniques, Ph.D. thesis, Univ. Montpellier, 1991, 187 pp.
[20] S. Rebaï, H. Philip, A. Taboada, Modern tectonic stress field in the Mediterranean region: evidence for variation in stress directions at different scales, Geophys. J. Int. 110 (1992) 106–140.
[21] M. Lejeune, Mémorial de la Nouvelle Triangulation Française, Institut Géographique National, Paris, 1950.
[22] G. Ferhat, Etude des déformations tectoniques actuelles des Alpes du Sud et la Provence à partir de la comparaison de réseaux de triangulation classique et satellitaire GPS (Global Positioning System), Ph.D. thesis, Univ. P. Sabatier, Toulouse, 1997, 257 pp.
[23] J. Chéry, C. Vigny, B. Meyer, G. Ferhat, M. Anzidei, R. Bayer, L. Boloh, P. Briole, A. Deschamps, K.L. Feigl, J.F. Gamond, A. Geiger, F. Jouanne, M. Kasser, M. Le Pape, J. Martinod, J.C. Ruegg, J.M. Scheubel, J.J. Walch, The western Alps covered by a high precision GPS network, Eos 76 (1995) 489.
[24] C. Luzet, Evolution du canevas géodésique national, état d'avancement du réseau géodésique français, Rev. XYZ 69 (1996), 55–61.
[25] R.W. King, Y. Bock, Documentation for the MIT GPS Analysis Software, GAMIT, Massachusetts Institute of Technology, Cambridge, 1997.
[26] Y. Bock, S.A. Gourevitch, C.C.C. III, R.W. King, R.I. Abbott, Interferometric analysis of GPS phase observations, Man. Geod. 11 (1986), 282–288.
[27] M. Rothacher, G. Beutler, E. Brockman, L. Mervat, S. Schaer, T.A. Springer, U. Wild, A. Wiget, C. Boucher, H. Seeger, Annual report 1995 of the CODE analysis center of the IGS, in: J.F. Zumberge, M.P. Urban, R. Liu, R.E. Neilan (Eds.), 1995 Annual Report, International GPS Service for Geodynamics, Pasadena, CA, 1996, pp. 151–173.
[28] D. Dong, The horizontal velocity field in southern California from a combination of terrestrial and space-geodetic data, Ph.D. thesis, Massachusetts Institute of Technology, Cambridge, 1993, 157 pp.
[29] D. Dong, T.A. Herring, R.W. King, Estimating regional deformation from a combination of space and terrestrial geodetic data, J. Geod. (1997), submitted.
[30] J.-J. Levallois, H. Monge, Géoïde européen version 1978, Institut Géographique National, Paris, 1978.
[31] G.W. Bawden, A. Donnellan, L.H. Kellogg, D. Dong, J.B. Rundle, Geodetic measurements of horizontal strain near the White Wolf fault, Kern County, California, 1926–1993, J. Geophys. Res. 102 (1997) 4957–4967.
[32] W.H. Prescott, J.C. Savage, W.T. Kinoshita, Strain accumulation in the western United States between 1970 and 1978, J. Geophys. Res. 84 (1979) 5423–5435.
[33] K.L. Feigl, R.W. King, T.H. Jordan, Geodetic measurement of tectonic deformation in the Santa Maria fold and thrust belt, California, J. Geophys. Res. 95 (1990) 2679–2699.
[34] F.C. Frank, Deduction of earth strains from survey data, Bull. Seismol. Soc. Am. 56 (1966) 35–42.
[35] J.C. Savage, R.O. Burford, Accumulation of tectonic strain in California, Bull. Seismol. Soc. Am. 60 (1970) 1877–1896.
[36] B. Grellet, P. Combes, T. Granier, H. Philip, Sismotectonique de la France Métropolitaine dans son cadre géologique et géophysique avec atlas de 23 cartes au 1/4.000.000ième et une carte au 1/1.000.000ième, Mém. Soc. Géol. Fr. 164 (1993) 76.
[37] A. Harmel, Etablissement d'un réseau géodésique de surveillance des mouvements de l'écorce terrestre. Méthodes terrestres et spatiales dans la région de la Basse et Moyenne Durance, Institut Géographique National, Paris, 1990.
[38] J.P. Masson, Sur l'amplitude du décrochement de la faille de Nîmes, déduite des variations de faciès barrémien-bédoulien, in: 8ème Réun. Ann. Sci. Terre, Marseille, 1980, p. 245.
[39] D. Carbon, P. Combes, M. Cushing, T. Granier, Enregistrement d'un paléoséisme dans les sédiments pléistocène de la vallée du Rhône, Géol. Alp. 69 (1993) 33–48.
[40] A. Ghafiri, Paléosismicité de failles actives en contexte de sismicité modérée: applications à l'évaluation de l'aléa sismique dans le sud-est de la France, Ph.D. thesis, Univ. Paris-Sud XI, 1995, 364 pp.
[41] C. Kerckhove, La zone du Flysch dans les nappes de l'Embrunais Ubaye (Alpes Occidentales), Géol. Alp. 45 (1969) 1–202.
[42] P. Labaume, J.F. Ritz, H. Philip, Failles normales récentes dans les Alpes sud-occidentales: leurs relations avec la tectonique compressive, C. R. Acad. Sci. Paris Sér. II 308 (1989) 1553–1560.
[43] J.F. Ritz, Tectonique récente et sismotectonique: analyse en termes de contraintes, Quaternaire 3 (1992) 111–124.

[44] B. Madeddu, N. Béthoux, J.-F. Stéphan, Champ de contrainte post-Pliocène et déformations récentes dans les Alpes du sud, Bull. Soc. Géol. Fr. 167 (1996) 797–810.

[45] M.P. Coward, D. Dietrich, Alpine tectonics — an overview, in: M.P. Coward, D. Dietrich, R.G. Park (Eds.), Alpine Tectonics, Geol. Soc. London, Spec. Publ. 45 (1989) 1–29.